Breaking Wave Interaction with a Vertical Cylinder and the Effect of Breaker Location

Arun Kamath*, Mayilvahanan Alagan Chella, Hans Bihs, Øivind A. Arntsen

Department of Civil and Environmental Engineering, Norwegian University of Science and Technology (NTNU), 7491 Trondheim, Norway

Ocean Engineering, 2016, **128** , pp. 105-115.
DOI: http://dx.doi.org/10.1016/j.oceaneng.2016.10.025

Abstract

The open-source CFD model REEF3D is used to simulate plunging breaking wave forces on a vertical cylinder. The numerical results are compared with data from the experiments carried out at the Large Wave Channel, Hannover, Germany to validate the model. Further, the location of the cylinder is changed so that the breaking wave impacts the cylinder at different stages of wave breaking and the resulting wave forces are evaluated. The different locations for the cylinder placement based on the breaker location are determined from the results obtained for the wave breaking process in a two-dimensional numerical wave tank. Maximum wave forces are found to occur when the breaking wave tongue impacts the cylinder just below the wave crest in all the cases simulated and the lowest wave forces are generally obtained when the wave breaks behind the cylinder. Several wave features such as the splashing on impact, the splitting and rejoining of the wave around the cylinder resulting in a chute-like jet formation are identified. The model provides a good representation of the breaking wave process and can be a useful tool to evaluate breaking wave forces on structures.

Keywords: breaking wave; wave forces; wave impact; vertical cylinder; Computational Fluid Dynamics; REEF3D Computational Fluid Dynamics; REEF3D

1 Introduction

A lot of research work has been carried out in the past on the evaluation of wave forces on structures exposed to waves due to their importance in coastal and offshore engineering. Wave interaction with a vertical circular cylinder depends on the Keulegan-Carpenter (KC) number and the relative size of the cylinder with respect to the incident waves. The KC number is a ratio between the excursion length of the fluid particles to the length of the obstacle in the

*Corresponding author, arun.kamath@ntnu.no
Postprint, published in Ocean Engineering, doi: http://dx.doi.org/10.1016/j.oceaneng.2016.10.025

flow. In the case of vertical circular cylinders in a wave field, it is given by KC $= uT/D$, where u is amplitude of the horizontal fludi velocity, T is the wave period and D is the diameter of the cylinder (Sumer and Fredsøe, 1997). The ratio measures the importance of the inertial forces and the drag forces. The wave forces on cylinders at higher KC numbers (KC > 2) and cylinder diameter to wavelength ratio $D/L < 0.2$ are generally determined using the Morison formula (Morison et al., 1950) to account for inertial and drag component of the wave forces using empirical force coefficients. In the case of breaking wave forces, the Morison formula cannot be directly applied because breaking waves are associated with impact forces of very high magnitudes acting over a short duration. In order to describe the total force from breaking waves with the Morison equation, an impact force term is considered in addition to the quasi-static forces (Goda et al., 1966). Present knowledge concerning the breaking wave forces is gained from experiments by Goda et al. (1966), Wienke and Oumeraci (2005), Arntsen et al. (2011) to name a few, but the measurement of velocity and acceleration under breaking waves and their interaction with structures is very demanding. The theoretical description of the impact force involves the use of several parameters such as slamming coefficients, curling factor, breaker shape and wave kinematics at breaking which have to be determined experimentally. Previous studies on breaking wave forces such as Chan and Melville (1988), Bullock et al. (2007), Wienke and Oumeraci (2005) have indicated that breaking wave impact characteristics depend on several parameters such as the depth inducing breaking, breaker type and the distance of the structure from the breaker location.

The modelling of breaking waves in shallow waters is challenging due to the complex nature of the physical processes including highly non-linear interactions. A considerable amount of numerical studies have been attempted to model wave breaking over plane slopes (Lin and Liu, 1998; Zhao et al., 2004; Alagan Chella et al., 2015*b*). These studies have helped extend the knowledge regarding breaking wave characteristics and the geometric properties of breaking waves. The quantification of these breaking wave parameters are an important input to improve the empirical coefficients used for the evaluation of breaking wave forces. Though many extensive numerical studies exist in current literature that study the wave breaking process, not many have been extended to study the forces due to breaking waves and the effect of breaker types on the wave forces. Bredmose and Jacobsen (2010) studied breaking wave impact forces due to focussed waves with the Jonswap wave spectrum for input and carried out computations for half the domain assuming lateral symmetry of the problem using OpenFOAM. Mo et al. (2013) measured and modelled solitary wave breaking and its interaction with a slender cylinder over a plane slope for a single case using the filtered Navier-Stokes equations with large eddy simulation (LES) turbulence modeling, also assuming lateral symmetry and showed that their numerical model sufficiently captured the important flow features. Choi et al. (2015) investigated breaking wave impact forces on a vertical cylinder and two cases of inclined cylinders for one incident wave using the modified Navier-Stokes equations with the volume of fluid (VOF) method for interface capturing to study the dynamic amplification factor due to structural response.

The study of breaking wave forces using computational fluid dynamics (CFD) can provide a very detailed description of the physical processes as the fluid physics are calculated with few assumptions. With high-order discretization schemes for the convection and time advancement, sharp representation of the free surface and tight velocity-pressure coupling in the model, the wave transformation, wave hydrodynamics and flow features can be represented very accurately and in a realistic manner. In the complex case of breaking wave interaction

with structures, CFD simulations can be used to capture the details of the flow field that are challenging to capture in experimental studies due to various factors including cost, instrumentation and structural response. Different wave loading scenarios can be analysed as the breaker locations are easier to analyse and maintain in the simulations.

In the current study, the open source CFD model REEF3D (Bihs et al., 2016) is used to simulate periodic breaking wave forces on a slender cylinder in a three-dimensional wave tank without assuming lateral symmetry. The model has been previously used to simulate the wave breaking process under different conditions (Alagan Chella et al., 2015*a*,*c*) and the wave breaking kinematics were fully represented including the motion of the jet, air pocket formation and the reconnection of the jet with the preceding wave trough. The model provides a detailed representation of the free surface and is numerically stable for various problems related to wave hydrodynamics. It is fully parallelised, has shown very good scaling on the high performance computing system at NTNU provided by NOTUR (2012) and can be used to carry out complex simulations efficiently on a large number of processors.

This paper presents the breaking wave interaction with a vertical cylinder. Three different wave heights are simulated and the evolution of wave breaking over a 1 : 10 slope is studied using two-dimensional simulations. The locations for the placement of the cylinder to investigate five different wave loading cases based on Irschik et al. (2002) are identified from these two-dimensional studies. Next, the wave forces in the different scenarios for the three different incident wave heights are evaluated in a three-dimensional numerical wave tank. The numerical model is validated by comparing the calculated wave forces and the free surface with experimental data from experiments carried out in the Large Wave Channel (GWK), Hannover, Germany. The wave interaction with the vertical cylinder in selected two different scenarios is investigated and the effect of the cylinder placement with respect to the breaker location on the free surface features is presented.

2 Numerical Model

The open-source CFD model REEF3D solves the fluid flow problem using the incompressible Reynolds-Averaged Navier-Stokes (RANS) equations along with the continuity equation:

$$\frac{\partial u_i}{\partial x_i} = 0 \tag{1}$$

$$\frac{\partial u_i}{\partial t} + u_j \frac{\partial u_i}{\partial x_j} = -\frac{1}{\rho}\frac{\partial p}{\partial x_i} + \frac{\partial}{\partial x_j}\left[(\nu + \nu_t)\left(\frac{\partial u_i}{\partial x_j} + \frac{\partial u_j}{\partial x_i}\right)\right] + g_i \tag{2}$$

where u is the velocity averaged over time t, ρ is the fluid density, p is the pressure, ν is the kinematic viscosity, ν_t is the eddy viscosity and g is the acceleration due to gravity.
The pressure is determined using Chorin's projection method (Chorin, 1968) and the resulting Poisson pressure equation is solved with a preconditioned BiCGStab solver (van der Vorst, 1992). Turbulence modeling is handled using the two-equation $k - \omega$ model proposed by Wilcox (1994), where the transport equations for the turbulent kinetic energy, k and the specific turbulent dissipation rate, ω are:

$$\frac{\partial k}{\partial t} + U_j \frac{\partial k}{\partial x_j} = \frac{\partial}{\partial x_j}\left[\left(\nu + \frac{\nu_t}{\sigma_k}\right)\frac{\partial k}{\partial x_j}\right] + P_k - \beta_k k\omega \tag{3}$$

$$\frac{\partial \omega}{\partial t} + U_j \frac{\partial \omega}{\partial x_j} = \frac{\partial}{\partial x_j}\left[\left(\nu + \frac{\nu_t}{\sigma_\omega}\right)\frac{\partial \omega}{\partial x_j}\right] + \frac{\omega}{k}\alpha P_k - \beta\omega^2 \tag{4}$$

$$\nu_t = \frac{k}{\omega} \tag{5}$$

where, P_k is the production rate and closure coefficients $\sigma_k = 2$, $\sigma_\omega = 2$, $\alpha = 5/9$, $\beta_k = 9/100$, $\beta = 3/40$.

The highly strained flow due to the propagation of waves in the tank results in an overproduction of turbulence in the numerical wave tank as the eddy viscosity is determined from the strain in the convective terms. The Bradshaw et al. (1967) assumption is used to limit the eddy viscosity as shown by Durbin (2009):

$$\nu_t \leq \sqrt{\frac{2}{3}}\frac{k}{|\mathbf{S}|} \tag{6}$$

where $\mathbf{S}$ stands for the source terms in the transport equations. In a two-phase CFD model, the large difference between the density of air and water leads to a large strain at the interface, which leads to an overproduction of turbulence at the free surface. In reality, the free surface is a boundary at which eddy viscosity is damped naturally which the standard $k-\omega$ model does not account for. In order to avoid the overproduction of turbulence at the free surface, the specific turbulence dissipation at the free surface is defined using the empirical relationship presented by Naot and Rodi (1982).

The discretization of the convective terms of the RANS equations are discretized using the fifth-order conservative finite difference Weighted Essentially Non-Oscillatory (WENO) scheme (Jiang and Shu, 1996). The Hamilton-Jacobi formulation of the WENO scheme (Jiang and Peng, 2000) is used to discretize the level set function ϕ, turbulent kinetic energy k and the specific turbulent dissipation rate ω. The WENO scheme is at minimum a third-order accurate scheme in the presence of large gradients and provides sufficient accuracy required to model complex free surface flows. The time advancement of the momentum equation, the level set function and the reinitialisation equation is treated with a Total Variation Diminishing (TVD) third-order Runge-Kutta explicit time scheme (Shu and Osher, 1988). The Courant-Frederick-Lewis (CFL) criterion is maintained at a constant value throughout the simulation using an adaptive time stepping strategy to determine the time steps. A first-order implicit scheme for the time advancement of k and ω removes the large source term contributions from these variables for the evaluation of the CFL criterion. This is reasonable, as these variables are largely driven by source terms and have a low influence from the convective terms. The diffusion terms of the velocities are also handled using an implicit scheme, removing them from the CFL criterion and the maximum velocities in the domain are used to determine the time steps to maintain the numerical stability of the simulation.

The model uses a Cartesian grid for spatial discretization and high-order finite difference schemes can be implemented in a straight forward manner. A ghost cell immersed boundary method (GCIBM) (Berthelsen and Faltinsen, 2008) is used to account for the complex geometric solid-fluid boundaries. The code is fully parallelised using the MPI library and the numerical model can be executed on high performance computing systems with very good scaling.

2.1 Level Set Method

The level set method (Osher and Sethian, 1988) is an interface capturing method in which the the zero level set of a signed distance function, $\phi(\vec{x}, t)$ represents the interface between two phases. For the rest of the domain, $\phi(\vec{x}, t)$ gives the closest distance of each point in the domain from the interface and the sign distinguishes the two phases across the interface. The level set function is continuous across the interface and is defined as:

$$\phi(\vec{x}, t) \begin{cases} > 0 & if\ \vec{x}\ is\ in\ phase\ 1 \\ = 0 & if\ \vec{x}\ is\ at\ the\ interface \\ < 0 & if\ \vec{x}\ is\ in\ phase\ 2 \end{cases} \tag{7}$$

The level set function provides a sharp representation of the interface. A partial differential equation based reinitialisation procedure presented by Peng et al. (1999) is used to maintain the signed distance property of the function, which can be lost on convecting the function under an external velocity field.

2.2 Numerical Wave Tank

The two-dimensional numerical wave tank has symmetry conditions on the side walls and the top of the tank. The bottom wall of the tank and boundaries of objects placed in the tank are treated with a no-slip or wall boundary condition. In a three-dimensional wave tank, the side walls are also subjected to wall boundary conditions. Wave generation is handled using the relaxation method (Larsen and Dancy, 1983), with the relaxation function presented by Jacobsen et al. (2012):

$$\Gamma(x) = 1 - \frac{e^{(1-x)^{3.5}} - 1}{e - 1} \tag{8}$$

where $\Gamma(x)$ is the relaxation function and $x \in [0, 1]$ is the length scale along the relaxation zone and ensures a smooth transition of the still water to a wave. The relaxation function also absorbs any waves reflected from the objects placed in the wave tank, travelling towards the wave generation zone. This prevents the reflected waves from affecting the wave generation and simulates a wave generator with active absorption. The numerical beach is implemented using the active absorbing beach formulated by Schäffer and Klopman (2000).

3 Results and Discussion

3.1 Setup for the numerical simulations

The experiments (Irschik et al., 2002) at the Large Wave Channel (GWK), Hannover are carried out in a wave channel 309 m long, 5 m wide and 7 m high with a 23 m long 1 : 10 slope reaching a height of 2.3 m placed at 180 m from the wavemaker. A flat bed extends from the end of slope with a height of 2.3 m. A vertical cylinder of diameter $D = 0.7$ m is placed with its central axis at the top of the slope and incident waves with heights H between $1.15 - 1.60$ m and periods T between $4.0 - 9.0$ s are generated. In the current study, the case with incident wave period $T = 4.0$ s, wave height $H = 1.30$ m and water depth $d = 3.8$ m presented in Choi et al. (2015) is chosen for comparison with the numerical

results. The three-dimensional numerical wave tank is 54 m long, 5 m wide and 7 m high with a grid size of $dx = 0.05$ m resulting a total of 15.12 million cells. In order to study the wave breaking process for the different cases simulated in the study, a two-dimensional wave tank with the same length and height is used as illustrated in Fig. (1). Waves with incident wave steepnesses $H_0/L_0 = 0.075, 0.070, 0.063, 0.059, 0.055$, corresponding to wave heights of $H_1 = 1.54$ m, $H_2 = 1.44$ m, $H_3 = 1.30$ m, $H_4 = 1.23$ m and $H_5 = 1.13$ m are generated to study the breaking wave forces on a vertical cylinder for different wave impact scenarios.

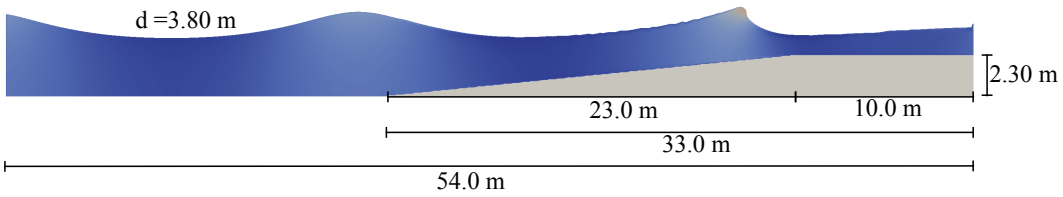

Figure 1: Dimensions of the two-dimensional numerical wave tank to determine breaking wave characteristics

3.2 Validation of the numerical model for breaking wave force calculation

The numerical results for breaking wave forces and the free surface elevation along the frontline of the cylinder ($x = 43.65$ m) near the tank wall for $H_3 = 1.30$ m are compared to the experimental data to validate the numerical model. The cylinder is placed with its axis at the top of the slope ($x = 44.00$ m), such that the front surface of the cylinder is directly at the breaking point and the vertical breaking wave crest impacts the cylinder front surface. A grid size of $dx = 0.05$ m is used. The filtered and Empirical Mode Decomposition (EMD)-treated experimental data from the experiments carried out at GWK, Hannover (Irschik et al., 2002), presented by Choi et al. (2015) is used for the comparison with the numerical results for the wave force. Figure (2a) shows that the numerical model provides a good prediction of the breaking wave force and the calculated wave force is consistent over several wave periods. Since the wave impact is very sensitive to the wave breaking location, the consistent results indicate that the model simulates successive breaking waves at the same location consistently. The numerically calculated free surface elevation along the frontline of the cylinder at $x = 43.65$ m also presents a good agreement with the experimental data in Fig. (2b) showing that the model provides a good representation of wave breaking in the wave tank.

A grid convergence study is carried out by repeating the above simulation with grid sizes of $dx = 0.20$ m, 0.15 m, 0.10 m, 0.025 m and compared to the results at $dx = 0.05$ m and experimental data for the wave force in Fig. (3). The results in Fig. (3a) show that the numerical values for the wave force at $dx = 0.025$ m and $dx = 0.05$ m converge to the experimental value. There is no significant improvement in the results for the wave forces when the grid size is improved from $dx = 0.05$ m to $dx = 0.025$ m. Figure (3b) shows the free surface elevation evaluated for the different grid sizes and for $dx = 0.15$ m and 0.20 m, neither the breaking location nor the vertical breaking crest is represented with sufficient accuracy. The wave forces calculated at these grid sizes are subsequently much lower as seen in Fig. (3a). At a grid size of $dx = 0.10$ m, the free surface differs slightly with regards

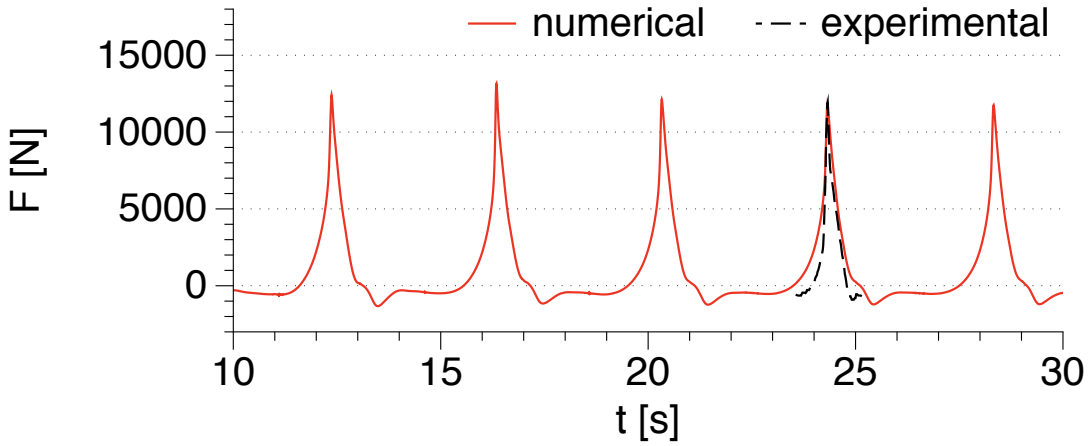

(a) wave force on the cylinder

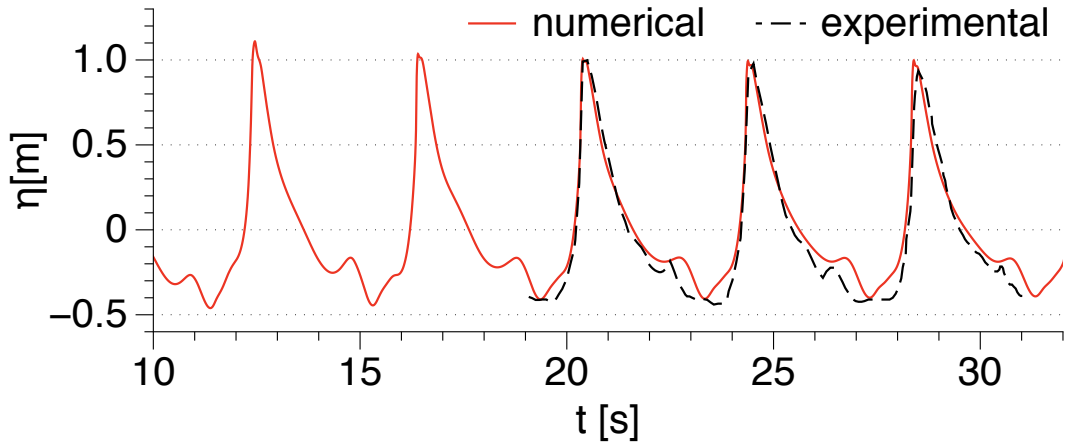

(b) free surface elevation at the tank wall, along the frontline of the cylinder

Figure 2: Comparison of numerical results with experimental data

to the breaking wave height but the corresponding difference in the calculated wave force is large. The vertical profile of the wave crest at breaking and the breaker location at $t = 24.3$ s is best represented by $dx = 0.05$ m. The horizontal and vertical components of the water particle velocity, u and w respectively, are calculated close to the wall along the frontline of the cylinder. The variation of u and w over time calculated on different grid sizes is presented in Figs. (3c) and (3d) respectively. It is seen that the water particle velocities converge for $dx = 0.05$ m. From the grid convergence studies, the grid size $dx = 0.05$ m is selected for all the simulations in this study. The breaking wave interaction in the numerical wave tank for the finest grid $dx = 0.025$ m with a total of 121 million cells is presented in Fig. (4). The high resolution simulation does provide more detailed flow features associated with the breaking process and the interaction with the cylinder, but the wave forces calculated on the cylinder are seen to be the same as that obtained using $dx = 0.05$ m.

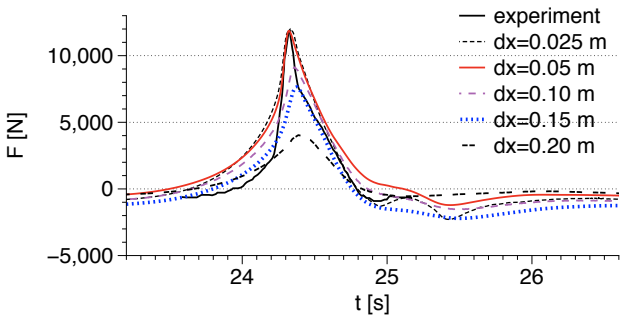

(a) calculated wave force

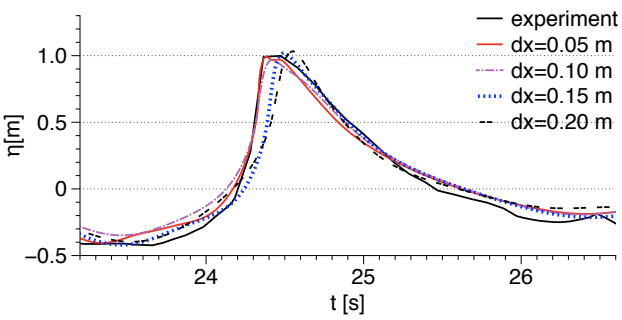

(b) calculated free surface elevation at $x = 43.65$ m

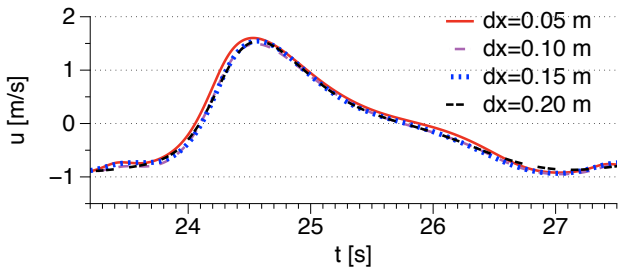

(c) calculated horizontal velocity u near the wall at $x = 43.65$ m and z/d=-0.13 m

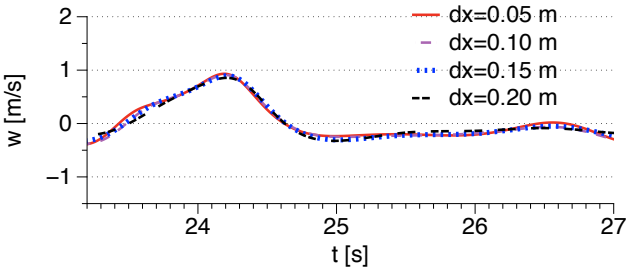

(d) calculated vertical velocity w near the wall at $x = 43.65$ m and z/d=-0.13 m

Figure 3: Grid convergence study for wave forces and free surface elevation near the wall along the frontline of the cylinder

3.3 Breaking wave characteristics

The characteristics of wave breaking for incident waves with period $T = 4.0$ s, wavelength $L = 20.53$ m and heights $H_1 = 1.54$ m, $H_2 = 1.44$ m, $H_3 = 1.30$ m, $H_4 = 1.23$ m and $H_5 = 1.13$ m is studied in a two-dimensional wave tank to identify the various stages of wave breaking. The results are used to select the locations to place the cylinder in order to analyse the effect of the wave breaker location on the wave force acting on the cylinder.

Similarly, simulations are carried out for the other incident waves simulated in this study and the breaking wave kinematics are analysed. The breaking point, the breaker depth index, the breaker height index and the breaking celerity are presented in Table (1). As the wave height decreases, waves break farther shoreward with relatively larger increase in the wave height at breaking (H_b) and the breaker depth index γ_b decreases. The waves break over the slope for H_1 and H_2 at the end of the slope for H_3 and on the flatbed for H_4 and H_5. Further, the value of the breaker height index Ω_b is almost 1.1 for all cases, implying that the wave height evolution is not strongly influenced by the incident wave characteristics.

Figure (5) depicts the free surface deformation and the evolution of the overturning wave crest of the plunging breaking waves over the slope along with the horizontal velocity contours for $H_3 = 1.30$ m. As a result of wave shoaling over the slope, the front face of the wave crest becomes steeper and the wave crest approaches a near-vertical profile in Fig. (5a). Due to increasing water particle velocities at the wave crest and reducing particle velocities

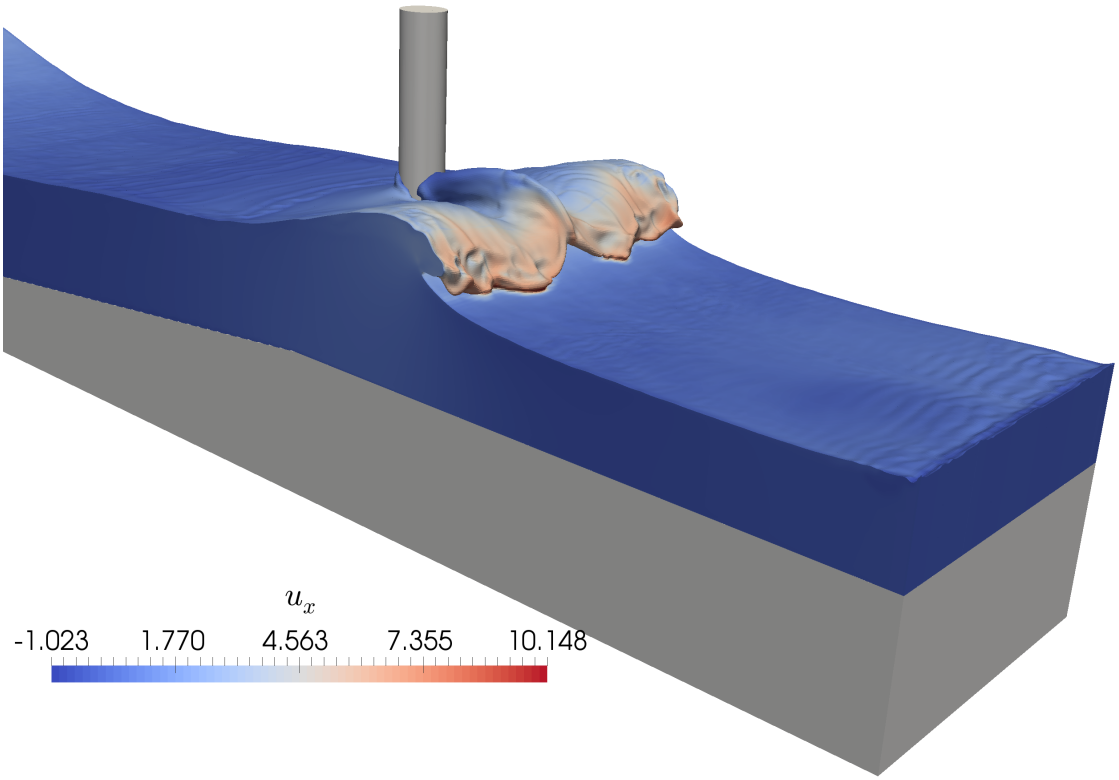

Figure 4: Breaking wave interaction with a vertical cylinder in the numerical wave tank with $dx = 0.025$ m and a total of 121 million cells showing the horizontal velocity contours

No.	incident wave height, H (m)	breaker height $H_b(m)$	breaking point x_b (m)	breaker depth index, γ_b	breaker height index, Ω_b
H_1	1.54	1.68	42.05	0.991	1.09
H_2	1.44	1.55	42.45	0.936	1.08
H_3	1.30	1.44	43.65	0.938	1.10
H_4	1.23	1.32	44.20	0.880	1.07
H_5	1.13	1.27	45.00	0.846	1.12

Table 1: Overview of the five different incident wave heights simulated and related breaking wave kinematics

towards the bed, the wave becomes asymmetrical and a part of the wave crest develops into an overturning crest seen in Fig. (5b). On further propagation, the overturning crest develops into a plunging jet which impinges the preceding wave trough, creating an air pocket, splash-up and secondary waves shorewards. The breaking characteristics vary depending on the incident wave characteristics, which determine the size and flow features of the overturning wave crest as seen in Figs. (5d-5f).

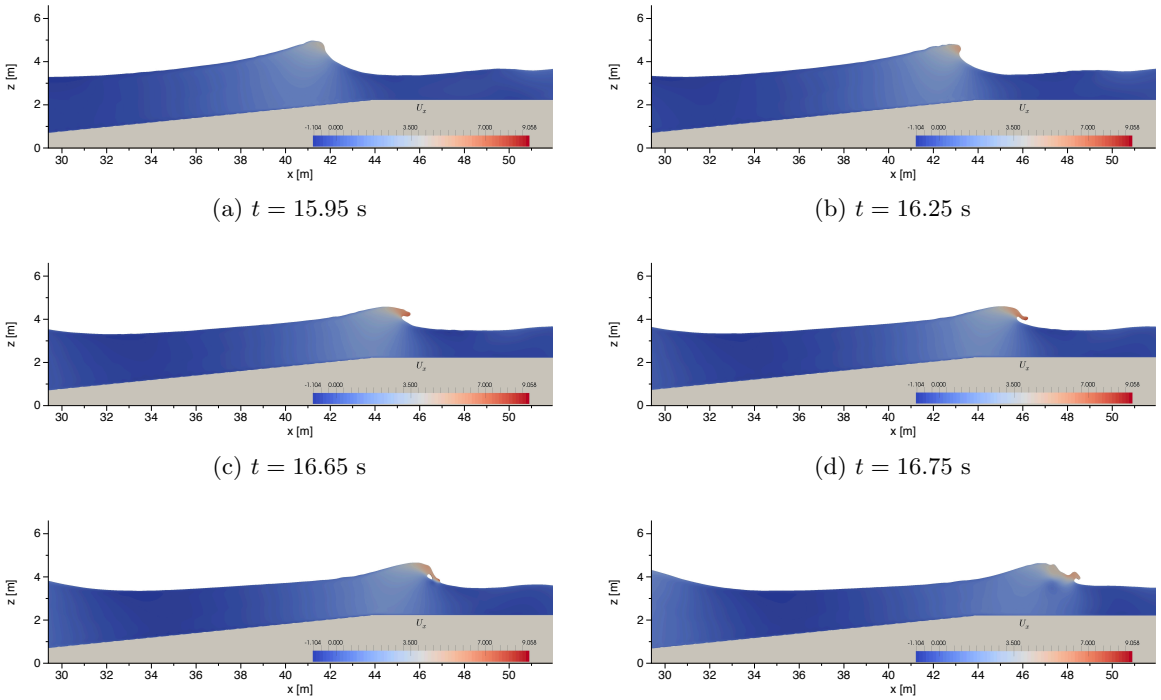

(a) $t = 15.95$ s

(b) $t = 16.25$ s

(c) $t = 16.65$ s

(d) $t = 16.75$ s

(e) $t = 16.90$ s

(f) $t = 17.25$ s

Figure 5: Evolution of the breaking wave for $H_B = 1.30$ m with horizontal velocity contours

3.4 Influence of cylinder location with respect to the breaker location

From the study about the breaking wave process for the five incident waves in section 3.3, five different locations at different stages of wave breaking are selected, similar to the loading cases identified in Irschik et al. (2002), as follows:

A. the wave breaks behind the cylinder, the crest is not yet vertical at impact.

B. the wave breaks exactly on the cylinder, the crest is vertical at impact.

C. the wave breaks just in front of the cylinder, the overturning wave crest impacts the cylinder at crest level

D. the wave breaks in front of the cylinder, the overturning wave crest impacts the cylinder slightly below the crest level

E. the wave breaks much before the cylinder, the overturning wave crest impacts the cylinder much below the crest level.

The different scenarios are illustrated in Fig. (6). An overview of the simulations carried out for the five different incident heights and the five different wave impact scenarios is listed in Table (2). The relative distance of the front surface of the cylinder from the breaking point is defined as

$$\tilde{x} = \frac{x_{cyl} - x_0}{L} \tag{9}$$

where x_{cyl} is the position of the front surface of the cylinder, x_0 is the wave breaking point and L is the incident wavelength. The values of $\tilde{x}$ and the corresponding calculated maximum breaking wave force for each simulation is presented in Table (2).

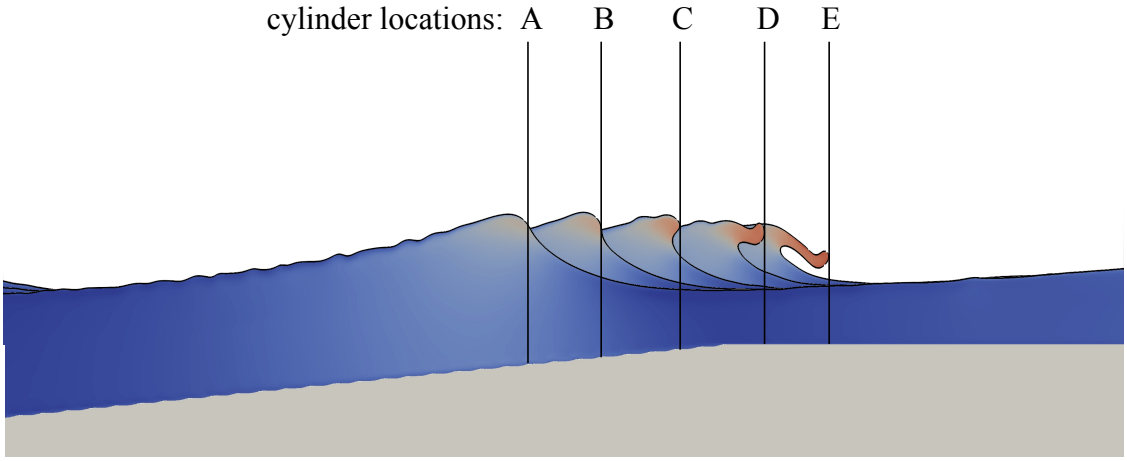

Figure 6: Location of the cylinder front surface for various wave loading cases

The calculated wave force on the cylinder in the different wave impact scenarios for different incident wave heights is presented in Fig. (7). The maximum breaking wave force for every incident wave height is generally obtained for the scenario D, where the overturning wave crest impacts the cylinder just below the wave crest. For incident wave height $H_1 = 1.54$ m, the maximum breaking wave force is calculated in scenario C where the overturning wave crest impacts the cylinder at crest level. This is justified as the impact scenarios C and D are close to each other. The maximum breaking wave force is calculated for these scenarios as the a large mass of water accelerating due to overturning of the wave crest impacts the cylinder surface. The lowest wave force is calculated in scenario A, where a steep non-breaking wave is incident on the cylinder surface. These findings are in agreement with previous studies for focussed waves and periodic waves (Wienke et al., 2000; Irschik et al., 2002).

The shape of the breaking wave force vs time plots are seen to be similar for a particular wave impact scenario for all the incident wave heights.In this case, the wave has not yet reached its breaking point and thus the impact scenario is different from the impact of an overturning wave crest. In scenario A, the wave force vs time plot does not have a distinctive peak due to the impact of the overturning wave crest. On the other hand, in case E, where the water mass from the broken wave crest and the trailing water mass impact the cylinder in succession, the breaking wave force plot shows a smaller peak just after the maximum force. The second peak results from the impact of the water mass that trails the overturning wave crest.

The variation of the maximum breaking wave forces with the relative distance of the cylinder from the wave breaking point ($\tilde{x}$) for the different incident waves is presented in Fig. (8a). It is seen that the breaking wave force on the cylinder for each incident wave increases as the cylinder is moved from before the wave breaking point to the position where the overturning wave crest impacts the cylinder just below the wave crest. The breaking wave force is reduced when the cylinder is moved further away from the breaking point and the overturning wave crest impacts the cylinder much below the wave crest level for every

No.	H (m)	x_b (m)	Cylinder axis (m)	$\tilde{x}$	F [N]
1A	1.54	42.05	40.35	-0.10	10510
1B			42.40	0.0	15070
1C			42.65	0.012	15460
1D			44.45	0.10	15010
1E			45.70	0.16	11520
2A	1.44	42.45	40.95	-0.09	10130
2B			42.80	0.0	12900
2C			43.05	0.012	12780
2D			44.85	0.10	14700
2E			46.25	0.16	10050
3A	1.30	43.65	42.70	-0.08	9470
3B			44.00	0.0	11090
3C			44.60	0.012	11500
3D			46.35	0.097	11600
3E			47.35	0.16	7580
4A	1.23	44.20	42.85	-0.08	8200
4B			44.55	0.0	9760
4C			45.15	0.03	10500
4D			46.60	0.10	10980
4E			47.85	0.16	10100
5A	1.13	45.00	43.80	-0.07	7600
5B			45.35	0.0	8540
5C			45.50	0.007	8620
5D			46.60	0.06	9270
5E			47.80	0.12	9130

Table 2: Overview of the simulations carried out to investigate the effect of different breaking wave impact scenarios

incident wave height. The dependence of the maximum breaking wave force on the relative distance $\tilde{x}$ is reduced as the incident wave height H is reduced for $\tilde{x} > 0$. For $H_1 = 1.54$ m, the maximum force at $\tilde{x} = 0.02$ is about 25% higher than the maximum force at $\tilde{x} = 0.16$. Whereas for $H_5 = 1.13$ m, the the maximum force at $\tilde{x} = 0.06$ is only 1.5% higher than the maximum force at $\tilde{x} = 0.12$.

The variation of the maximum wave breaking force in the different scenarios of wave impact for the different incident wave heights is shown in Fig. (8b). Here, it is clearly seen that the wave force is increased with increasing incident wave height for every wave impact scenario. The maximum wave forces in scenario A are the lowest for all the incident wave heights and the highest for scenario D. For scenario A, where a steep non-breaking wave impacts the cylinder, the increase in the maximum wave force as H is increased from 1.13 m to 1.54 m is 38%. For scenarios B, C and D where the the overturning wave crest impacts the cylinder the maximum breaking wave forces increases by $62 - 80\%$. In the case of scenario E, where a fully developed overturning wave crest impacts the cylinder just before splash up, the increase in the maximum wave forces in just 27%.

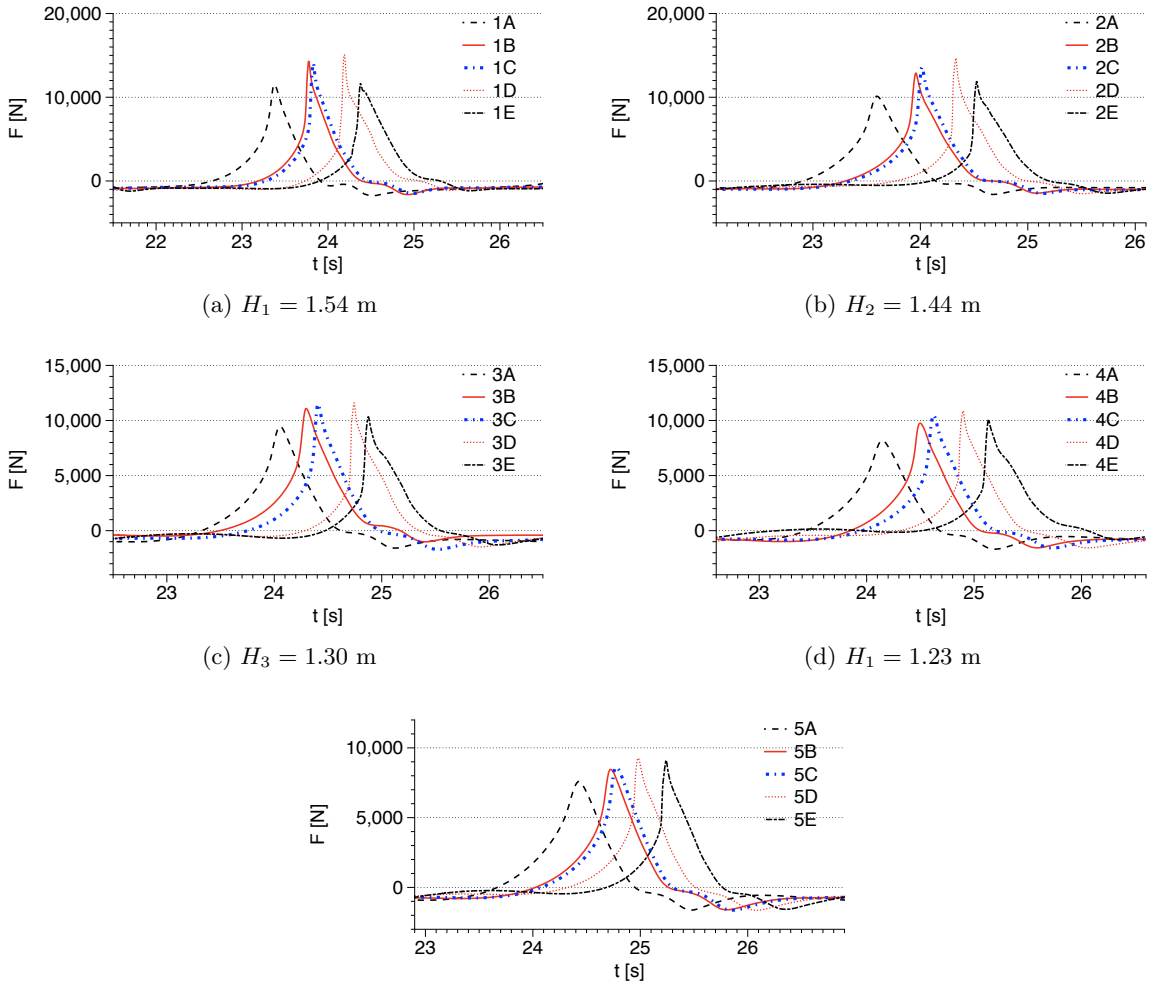

(a) $H_1 = 1.54$ m

(b) $H_2 = 1.44$ m

(c) $H_3 = 1.30$ m

(d) $H_1 = 1.23$ m

(e) $H_1 = 1.13$ m

Figure 7: Breaking wave forces in different scenarios A-E for different incident wave heights $H_1 - H_5$

In order to further analyse the breaking wave force characteristics, the rise time (t_r) is calculated for the different breaking scenarios and presented in Fig. (9). The relative rise times are obtained by normalised the values with the total duration of the wave impact in each case. The relative rise times (t_r/t_d) for the different incident wave heights over different wave impact scenarios are presented in Fig. (9a). The highest relative rise times are calculated for the the lowest wave height simulated, $H_5 = 1.13$ m, while the lowest relative rise times are calculated for the highest wave height simulated, $H_1 = 1.54$ m. This suggests that a shorter relative rise time in the wave force plot leads to a higher breaking wave force. The relative rise time is strongly influenced by $\tilde{x}$ for the higher incident wave heights and t_r reduces as $\tilde{x}$ increases.

Figure (9b) shows the variation of the relative rise times over the incident wave height for different wave impact scenarios. Scenario A, where a steep wave impacts the cylinder

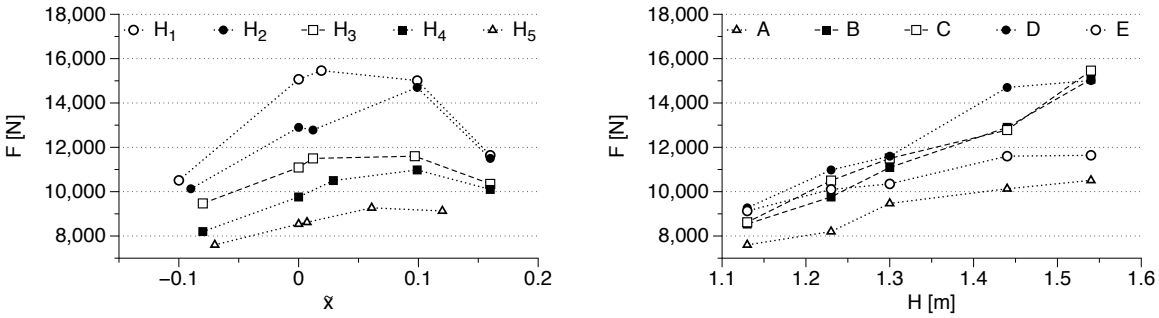

(a) variation of maximum breaking wave force with distance from breaking point for different inicdent wave heights

(b) variation of maximum breaking wave force with wave height for various impact scenarios

Figure 8: Variation of the maximum breaking wave force with distance of cylinder front surface from the wave breaking point

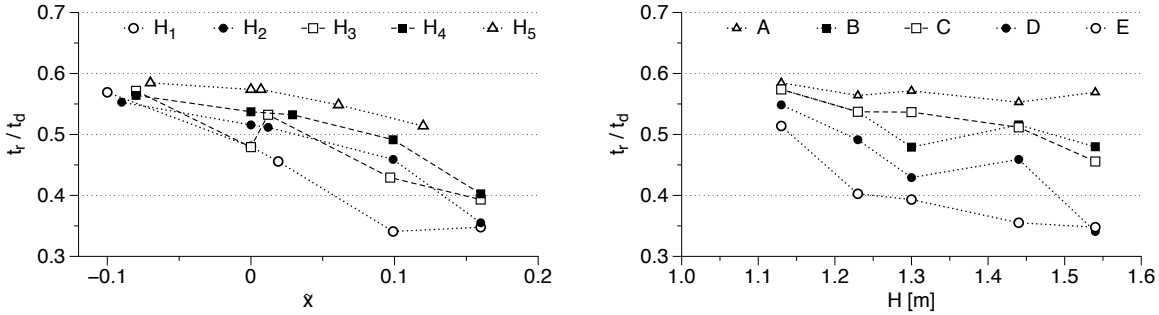

(a) variation of maximum breaking wave force with distance from breaking point for different incident wave heights

(b) variation of maximum breaking wave force with wave height for various impact scenarios

Figure 9: Variation of breaking wave force rise time and total time of impact in the different scenarios

before the onset of wave breaking has the highest relative rise times for every incident wave height simulated and t_r is about $55-58\%$ of the total duration. The lowest rise times are calculated for scenario E, where a broken wave impacts the cylinder, with t_r being $34-50\%$ of the total duration. It is noted that though the relative rise times are small, the breaking wave forces calculated for this scenario are quite low as seen in Fig. (8b). Scenario D, the scenario where the highest breaking wave forces are obtained has the second lowest relative rise times and t_r is about $55-34\%$ of the total duration. This observation can be justified as follows. The breaking wave forces are generally higher when the relative rise times are lower. An exception is observed when the wave impact on the cylinder is due to a fully developed overturning wave crest in scenario E. The wave impact occurs when the overturning wave crest is about to rejoin the preceding wave crest and just before the splash up phenomenon after wave breaking. This leads to a longer total duration of the impact and thus the values of relative rise times are lower. The water mass impacting the cylinder is also lower in scenario E compared to scenario D and thus the resulting maximum breaking wave forces are lower.

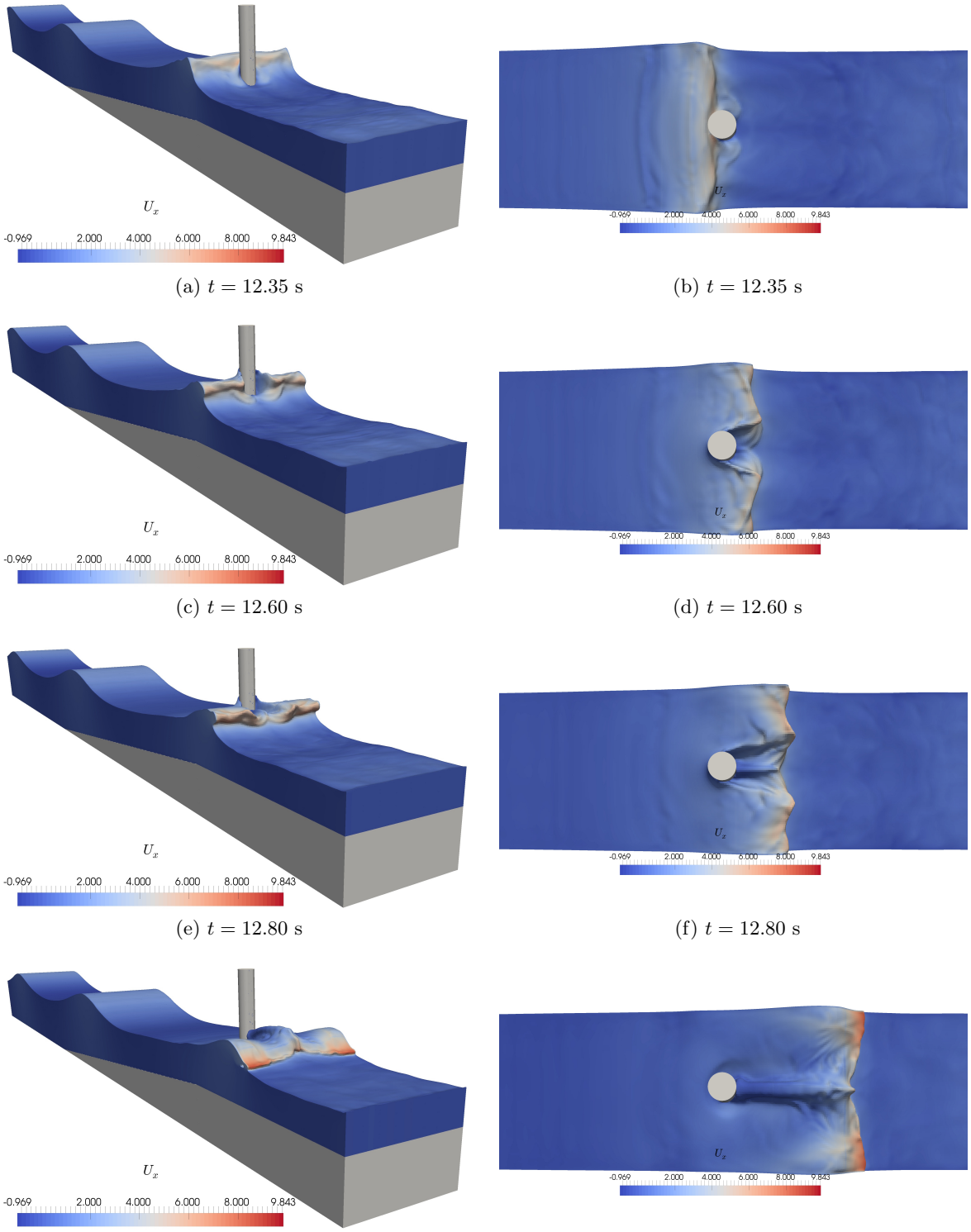

(a) $t = 12.35$ s (b) $t = 12.35$ s

(c) $t = 12.60$ s (d) $t = 12.60$ s

(e) $t = 12.80$ s (f) $t = 12.80$ s

(g) $t = 13.25$ s (h) $t = 13.25$ s

Figure 10: Isometric and corresponding top views of breaking wave interaction with the cylinder for $H_B = 1.30$ m for scenario 3B

In order to obtain more insight into the difference in the physical free surface features in two different wave impact scenarios, the breaking wave interaction with the cylinder in 3B and 3E are presented and the free surface features are discussed. Figure (10) presents the interaction process for case 3B, where the wave impacts the cylinder at the breaker location with both isometric view of the tank and the top view around the cylinder. The wave crest front profile is vertical during incidence on the cylinder front surface in Fig. (10a). The wave crest begins to overturn as it passes the cylinder in Figs. (10c and 10d). The separation of the incident wavefront by the cylinder and the generation of semi-circular waves meeting in the shadow zone behind the cylinder is seen in Fig. (10d). The meeting of the semi-circular wavefronts behind the cylinder and the formation of a chute-like jet is seen in Fig. (10f). The chute-like jet originates in the region of low horizontal velocities behind the cylinder and has a maximum horizontal velocities at the tip, where it meets the broken wave crest. Figure (10g) shows the fully developed chute-like jet and is seen to extend up to just behind the broken wave crest in Fig. (10h). The chute-like jet appears after the peak force is observed for the cylinder and thus may not have a significant effect on the forces experienced by the cylinder. The importance of the chute-like jet may be more apparent in the case of neighboring cylinders placed in the zone of influence of the chute-like jet behind the first cylinder. The chute-like jet can lead to a large wave run-up on the downstream cylinder. It can also result in interaction effects between the cylinders based on the distance between the two cylinders, influencing the wave forces on both cylinders.

The free surface features associated with the breaking wave interaction in case 3E is presented in Fig. (11) shows the interaction of a fully developed overturning wave crest with the cylinder. The highly curled wave crest impacts the cylinder much below the wave crest level in Fig. (11a). Figure (11c) shows the separation of the incident wavefront. Semi-circular wavefronts meeting behind the cylinder seen for 3B is not seen in here in Fig. (11d). The broken wave separated around the cylinder propagates further with a region of low velocity in the shadow region behind the cylinder in Fig. (11e). There are no major free surface features at this stage in Fig. (11f). A mildly developed chute-like jet is seen in Fig. (11g) which is close to its collapse state and this weakly developed chute wave is seen to rejoin the free surface at some distance behind the broken wave crest in Fig. (11h).

From the two different wave impact scenarios presented, the wave interaction process with the cylinder varies for the two cases in terms of free surface features and the velocities around the cylinder. When the wave impacts the cylinder at its breaking point, in case 3B, major free surface features are noticed in the shadow region behind the cylinder, with the development of a strong chute-like jet which extends up to the broken wave crest. Semi-circular waves are formed just behind the cylinder, which meet in the shadow region and result in the chute-like jet. When the overturning wave impacts the cylinder with the overturning wave crest much below the wave crest in case 3E, the separation of the wavefront occurs without major free surface features in the region behind the cylinder. The chute-like jet is developed at a late stage is also seen to be weaker than in the previous scenario with regards to both the velocity of the chute tip and the length of extension.

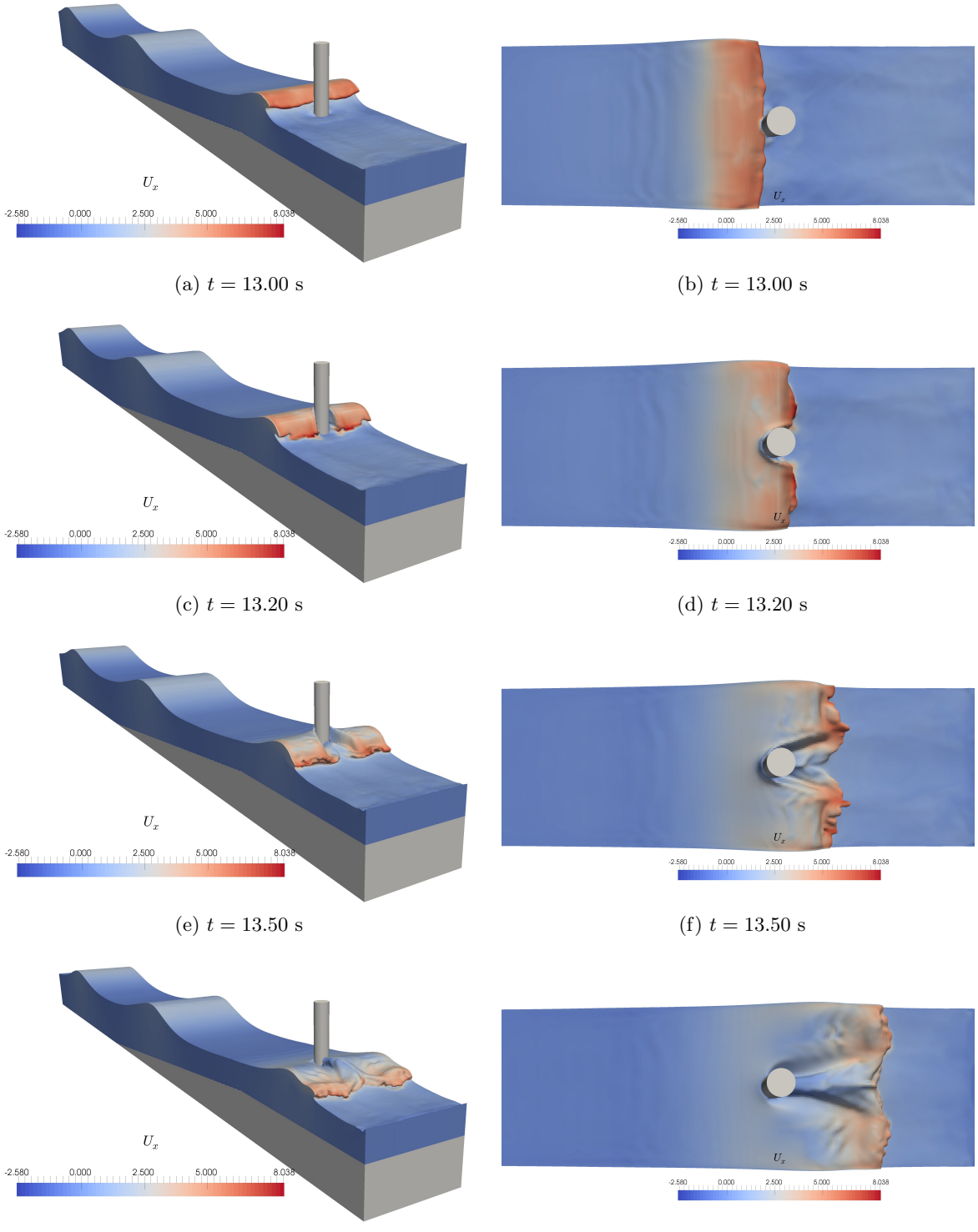

(a) $t = 13.00$ s (b) $t = 13.00$ s

(c) $t = 13.20$ s (d) $t = 13.20$ s

(e) $t = 13.50$ s (f) $t = 13.50$ s

(g) $t = 13.85$ s (h) $t = 13.85$ s

Figure 11: Isometric and corresponding top views of breaking wave interaction with the cylinder for $H_B = 1.30$ m for scenario 3E

4 Conclusions

The open-source CFD model REEF3D is used to simulate breaking wave interaction with a vertical cylinder. The effect of different incident wave heights and different wave impact scenarios for each incident wave height is studied by changing the location of the cylinder. The process of wave breaking is first studied using two-dimensional simulations. The cylinder locations for different wave impact scenarios are identified from these simulations. The numerical results for the wave force and the free surface elevation are compared to experimental data from large scale tests carried out at the Large Wave Channel, Hannover, Germany and a good agreement is obtained. The following conclusions can be drawn from the studies carried out in this study:

- The location of the cylinder with respect to the wave breaking point has a large influence on the breaking wave forces. This influence is more significant for higher incident waves.
- The highest force is generally seen in the scenario where the overturning wave crest impacts the cylinder just below the wave crest level and the lowest force is obtained when the wave breaks behind the cylinder.
- The breaking wave force is generally seen to be higher when the rise time relative to the total duration of impact is lower. An exception is seen when a fully developed overturning wave crest impacts the cylinder, where the wave forces are lower in spite of lower relative rise times.
- The relative rise time is strongly influenced by the location of the cylinder with respect to the breaking point for higher incident wave heights. The relative rise time and the distance of the cylinder from the breaking point are inversely related.
- Different free surface features are observed in the different scenarios presented. The formation of a chute-like jet is seen in the shadow region behind the cylinder, where the wavefront split by the cylinder partly reunites. The chute-like jet is less developed and extends to a smaller distance when the wave impacts the cylinder at a later stage of breaking.

The current study has presented several interesting results for breaking wave interaction with vertical slender cylinders. The results can be used to extend the knowledge regarding breaking wave forces to the complex scenario of breaking wave interaction with tripod and truss structures.

Acknowledgements

This study has been carried out under the OWCBW project (No. 217622/E20) and the authors are grateful to the grants provided by the Research Council of Norway. This study was supported in part with computational resources at the Norwegian University of Science and Technology (NTNU) provided by NOTUR, http://www.notur.no (NN2620K).

References

Alagan Chella, M., Bihs, H. and Myrhaug, D. (2015*a*). Characteristics and profile asymmetry properties of waves breaking over an impermeable submerged reef. *Coastal Engineering*, **100**, 26–36.

Alagan Chella, M., Bihs, H., Myrhaug, D. and Muskulus, M. (2015*b*). Breaking characteristics and geometric properties of spilling breakers over slopes. *Coastal Engineering*, **95**, 4–19.

Alagan Chella, M., Bihs, H., Myrhaug, D. and Muskulus, M. (2015*c*). Hydrodynamic characteristics and geometric properties of plunging and spilling breakers over impermeable slopes. *Ocean Modelling, Virtual Special Issue: Ocean Surface Waves*, 1–20.

Arntsen, Ø.A., Ros, X. and Tørum, A. (2011). Impact forces on a vertical pile from plunging breaking waves. In: *Coastal Structures*.

Berthelsen, P.A. and Faltinsen, O.M. (2008). A local directional ghost cell approach for incompressible viscous flow problems with irregular boundaries. *Journal of Computational Physics*, **227**, 4354–4397.

Bihs, H., Kamath, A., Alagan Chella, M., Aggarwal, A. and Arntsen, Ø.A. (2016). A new level set numerical wave tank with improved density interpolation for complex wave hydrodynamics. *Computers & Fluids*. 10.1016/j.oceaneng.2016.10.02510.1016/j.compfluid.2016.09.012.

Bradshaw, P., Ferriss, D.H. and Atwell, N.P. (1967). Calculation of boundary layer development using the turbulent energy equation. *Journal of Fluid Mechanics*, **28**, 593–616.

Bredmose, H. and Jacobsen, N.G. (2010). Breaking wave impacts on offshore wind turbine foundations: focused wave groups and CFD. *Proc., 29th International Conference on Ocean, Offshore and Arctic Engineering, Shanghai, China*.

Bullock, G.N., Obhrai, C., Peregrine, D.H. and Bredmose, H. (2007). Violent breaking wave impacts. part 1: Results from large-scale regular wave tests on vertical and sloping walls. *Coastal Engineering*, **54**(8), 602–617.

Chan, E.S. and Melville, W.K. (1988). Deep-water plunging wave pressures on a vertical plane wall. In: *Proc. of the Royal Society of London. A. Mathematical and Physical Sciences*, volume 417, 95–131.

Choi, S.J., Lee, K.H. and Gudmestad, O.T. (2015). The effect of dynamic amplification due to a structure s vibration on breaking wave impact. *Ocean Engineering*, **96**, 8–20.

Chorin, A. (1968). Numerical solution of the Navier-Stokes equations. *Mathematics of Computation*, **22**, 745–762.

Durbin, P.A. (2009). Limiters and wall treatments in applied turbulence modeling. *Fluid Dynamics Research*, **41**, 1–18.

Goda, Y., Haranaka, S. and Kitahata, M. (1966). Study on impulsive breaking wave forces on piles. *Report Port and Harbour Technical Research Institute*, **6**(5), 1–30.

Irschik, K., Sparboom, U. and Oumeraci, H. (2002). Breaking wave characteristics for the loading of a slender pile. In: *Proc. 28th International Conference on Coastal Engineering, Cardiff, Wales.*

Jacobsen, N.G., Fuhrman, D.R. and Fredsøe, J. (2012). A wave generation toolbox for the open-source CFD library: OpenFOAM. *International Journal for Numerical Methods in Fluids*, **70**(9), 1073–1088.

Jiang, G.S. and Peng, D. (2000). Weighted ENO schemes for Hamilton-Jacobi equations. *SIAM Journal on Scientific Computing*, **21**, 2126–2143.

Jiang, G.S. and Shu, C.W. (1996). Efficient implementation of weighted ENO schemes. *Journal of Computational Physics*, **126**, 202–228.

Larsen, J. and Dancy, H. (1983). Open boundaries in short wave simulations - a new approach. *Coastal Engineering*, **7**, 285–297.

Lin, P. and Liu, P.L.F. (1998). A numerical study of breaking waves in the surf zone. *Journal of Fluid Mechanics*, **359**, 239–264.

Mo, W., Jensen, A. and Liu, P.L.F. (2013). Plunging solitary wave and its interaction with a slender cylinder on a sloping beach. *Ocean Engineering*, **74**, 48–60.

Morison, J.R., O'Brien, M.P., Johnson, J.W. and Schaaf, S.A. (1950). Force exerted by surface waves on piles. *Journal of Petroleum Technology*, **2**, 149–154.

Naot, D. and Rodi, W. (1982). Calculation of secondary currents in channel flow. *Journal of the Hydraulic Division, ASCE*, **108**(8), 948–968.

NOTUR (2012). The Norwegian Metacenter for Computational Science. *http://www.notur.no/hardware/vilje.*

Osher, S. and Sethian, J.A. (1988). Fronts propagating with curvature- dependent speed: algorithms based on Hamilton-Jacobi formulations. *Journal of Computational Physics*, **79**, 12–49.

Peng, D., Merriman, B., Osher, S., Zhao, H. and Kang, M. (1999). A PDE-based fast local level set method. *Journal of Computational Physics*, **155**, 410–438.

Schäffer, H.A. and Klopman, G. (2000). Review of multidirectional active wave absorption methods. *Journal of Waterway, Port, Coastal, and Ocean Engineering*, **126**(2), 88–97.

Shu, C.W. and Osher, S. (1988). Efficient implementation of essentially non-oscillatory shock capturing schemes. *Journal of Computational Physics*, **77**, 439–471.

Sumer, B.M. and Fredsøe, J. (1997). *Hydrodynamics around cylindrical structures.* Vol. 12. World Scientific.

van der Vorst, H. (1992). BiCGStab: A fast and smoothly converging variant of Bi-CG for the solution of nonsymmetric linear systems. *SIAM Journal on Scientific and Statistical Computing*, **13**, 631–644.

Wienke, J. and Oumeraci, H. (2005). Breaking wave impact force on a vertical and inclined slender pile – theoretical and large-scale model investigations. *Coastal Engineering*, **52**, 435–462.

Wienke, J., Sparboom, U. and Oumeraci, H. (2000). Breaking wave impact on a slender cylinder. In: *Coastal Engineering Conference*, volume 2, 1787–1798.

Wilcox, D.C. (1994). *Turbulence modeling for CFD.* DCW Industries Inc., La Canada, California.

Zhao, Q., Armfield, S. and Tanimoto, K. (2004). Numerical simulation of breaking waves by a multi-scale turbulence model. *Coastal Engineering*, **51**(1), 53–80.